Mo-substitution in V_2O_5 tunes the structure towards three-dimensional connectivity and improves Li-ion battery cycling

Kausturi Parui,[†] Bonnie G. Gardner,[‡] Kathryn A. Pitton,[¶] Noah G. Caracuel,[†] Emily Vidal-Torres,[†] Shornam Gandhi,[†] Beth S. Guiton,[¶] Juan C. Nino,[†] and Megan M. Butala[*,†]

†*Department of Materials Science and Engineering, University of Florida, Gainesville, FL 32611, USA*

‡*Department of Chemical Engineering and Materials Science Department, Michigan State University, East Lansing, MI, 48910, USA*

¶*Department of Chemistry, University of Kentucky, 125 Chemistry-Physics Building,Lexington, KY, 40506-0055, USA*

E-mail: mbutala@ufl.edu

Abstract

The development of alternative energy sources is crucial for reducing reliance on fossil fuels, particularly for mobile applications such as personal electronics and transportation. This necessitates the advancement of battery materials based on abundant and inexpensive constituent elements. To achieve this requires investigating materials in a broader compositional and structural design space. Early transition metal oxides, including the intercalation electrode $\alpha-V_2O_5$, however, the performance of V_2O_5 is hindered by phase transformations during battery cycling that lead to capacity fade

and short device lifetimes. This study investigates the modification of V_2O_5 through Mo substitution in a series of the form $V_{2-x}Mo_xO_5$ for x = 0.05, 0.1, 0.2, 0.4, 0.6, and 0.8. X-ray diffraction data reveal progressive structural changes with increasing Mo content, which in turn change the progression of phase transformations during the first discharge. The different product also results in different cycling profile shapes that indicate differences in the charge storage mechanism as a function of Mo content. As a result, samples with higher Mo-substitution, especially $V_{1.2}Mo_{0.8}O_5$, have narrower hysteresis, higher capacity, and improved capacity retention. While there is a limited solubility of Mo in the V_2O_5 structure, with secondary phases and defects at many compositions, we show that Mo substitution alters the cycling behavior of V_2O_5 to deep discharge, which can inform the design of intercalation materials for energy storage applications.

Introduction

Enabling alternative sources of energy is essential for reducing dependence on fossil fuels.[1] For mobile applications, such as personal electronics and for transportation, this requires the continued development of battery materials, especially those based on abundant and low cost materials.[2] In addition to identifying specific materials candidates for commercialization, there is also a need to expand our understanding of fundamental structure-property relationships affecting energy and power densities, as well as long-term cycling performance of battery electrode materials.[3,4]

While there is robust understanding of conventional Li-ion battery cathodes, such as layered oxides based on Co, Ni, Mn, and Al, a broader compositional and structural design space will benefit the development of sustainable long-term energy solutions.[5–8] A promising class of alternative materials comprises early transition metal oxides,[7,9–12] including classic intercalation electrode $\alpha-V_2O_5$.[13–16] Interest in V_2O_5 is related to its high capacity, about 450 $mAh\,g^{-1}$, however, its commercial adoption for energy storage is prevented by

the cascade of phase transformations that accompany the coupled insertion (and removal) of Li-ions and electrons during battery cycling. These phase transformations alter the Li transport pathways and over time cause particle fracture, resulting in significant capacity fade and short device lifetimes.[17–19] Thus, there have been many efforts to understand the nature of the phase transformations in V_2O_5 and how to mitigate them, including through nanostructuring, compositional design, and electrode processing (*e.g.*, carbon-coating).[14,20]

The α polymorph of V_2O_5 is composed of layers of [VO_5] square pyramids (Fig. 1a). These square pyramids alternate being corner- and edge-sharing, arranging into slabs that are two corner-sharing polyhedra wide and connected by edge-sharing polyhedra. The structure can also be viewed as rugged layers, across which there are long V−O interatomic distances. As guest Li ions are intercalated between the complex layers in V_2O_5, the square pyramids rotate around corner sharing vertices, resulting in a series of phase transformations as Li content changes, progressing through the α, ϵ, δ, and γ phases of V_2O_5.[18,21,22] During discharge to potentials of 1.9 V or lower, a disordered rocksalt ω polymorph forms, with an estimated composition of $Li_3V_2O_5$.[15,23,24]

Modification of the V_2O_5 structure and cycling behavior has been explored, including through substitution of V by other transition metals and by the addition of other species in the interlayer space, including Na^+, K^+, and NH_4^+.[21,25,26] These changes have been reported to alter the layered structure, including the relative orientations of square pyramids and the interlayer spacing.[21,27] In addition, substitution of V by other species, of the form $V_{2-x}M_xO_5$, has been shown to result in changes in cycling behavior, including for $M = Al^{3+}$, Mn^{2+}, and Mo^{6+}.[14,27–30] The mechanism of incorporation of lower valent Al and Mn remains unclear, especially charge compensation and whether these species are incorporated between or within layers. In contrast, more is known about substitution of V by Mo, including reported atomic structures for several Mo concentrations.[24,27,31–34] In addition, chemical characterization has indicated that Mo is incorporated in its 6+ oxidation state, meaning there is some reduction of V^{5+} to V^{4+}, which has a larger ionic radius.[35,36]

Despite previous reports of the structures of $V_{2-x}Mo_xO_5$ for $0 < x \leq 0.9$,[24,31–33] recent work indicates a lower solubility limit of Mo in V_2O_5.[27] Specifically, Schofield *et al.* report substitution in the range $0 < x \leq 0.147$, beyond which secondary phases form. In this narrow substitution range, their data show a decrease in the interlayer spacing with increasing Mo content, as well as associated improvements in battery cycling behavior, especially reversibility of two-phase transformations when cycled to a lower potential of 2 V.[27] For low Mo concentrations, they find that Mo content drives a 'pre-transformation' that reduces the mechanical strain that typically occurs during the initial stages of lithiation, which alleviates some of the associated issues of particle fracture.

In previous work that reports Mo substitution up to $V_{1.1}Mo_{0.9}O_5$ (Fig 1c), a decrease in interplanar spacing is also reported.[24,32,35] Duc *et al.* suggest that Mo^{6+} substitution for V^{5+} has an associated reduction of some V to the larger 4+ ion. They attribute the combination of larger Mo^{6+} and V^{4+} toward a more octahedral coordination,[32] shortening the long interlayer V−O distance and shifting the structure from the original layered structure of $\alpha-V_2O_5$ toward the more three-dimensional structure of 'idealized' V_2O_5. In these higher Mo-substituted samples, structural change toward a more three-dimensional structure have been reported to alter the electrochemical and electrochromic behavior relative to V_2O_5.[24,27,31–33]

The structural progression from square-pyramidal toward an octahedral coordination with Mo-substitution has the potential to improve the cycling behavior in V_2O_5.[12,21,32] For example, the R polymorph of Nb_2O_5, which has the idealized V_2O_5 structure (Fig. 1d),[37] shows only minor structural changes with cycling, resembling the highly stable Wadsley−Roth materials despite its structural similarity to V_2O_5.[12]

Given the relationship between V_2O_5 and $R-Nb_2O_5$, we report here the degree to which idealization can be achieved in V_2O_5 through Mo-substitution and the associated effects on electrochemical lithiation and delithiation. Specifically, we assess changes in the phase transformations during lithiation that result from Mo-substitution, and whether the stable cycling

and excellent rate capabilities of Wadsley−Roth materials can be achieved in materials based on V.

We find that X-ray diffraction (XRD) data of a solvothermally prepared series of Mo-substituted V_2O_5 indicate progressive structural differences with increasing Mo content. The resulting changes in the V_2O_5 structure prompt an alternative progression of phase transformations during the first discharge. In all compositions we study, cycling data suggest that with increased Mo content the atomic structure evolution is significantly changed during the first discharge. Cycling to a deep discharge, the phase transformations during the first discharge are not reversible, suggesting the formation of a disordered rocksalt structure, such as $\omega-Li_3V_2O_5$.[24] The differences in the structure and chemistry of the first discharge product result in narrower hysteresis, higher capacity, and improved capacity retention for V_2O_5 with high Mo-substitution, especially $V_{1.2}Mo_{0.8}O_5$.

However, Mo substitution is limited by the preferential formation of other Mo-V-O phases, and hence idealization does not seem possible, even through low-temperature synthesis routes. Even though the composition range of phase purity is narrow, samples with higher Mo content and, with secondary phase(s) show improved electrochemical cycling behavior. However, the current study is not able to identify the origin of this difference or the nature of the cycling products, but such future work could be of interest to facilitate crystallographic design of intercalation materials for energy storage and other functional applications.[38–42]

Methods

Synthesis

$V_{2-x}Mo_xO_5$ powders with $x = 0.05$, 0.1, 0.15, 0.2, 0.4, 0.6, 0.8 were synthesized via solvothermal methods using a temperature-controlled autoclave (Model 4768 General Purpose Vessel, 600 mL, Parr Instrument Company) adapted from previous literature report.[31] Two precursor solutions, one for V and one for Mo, were separately prepared. For the V solution, triethylene

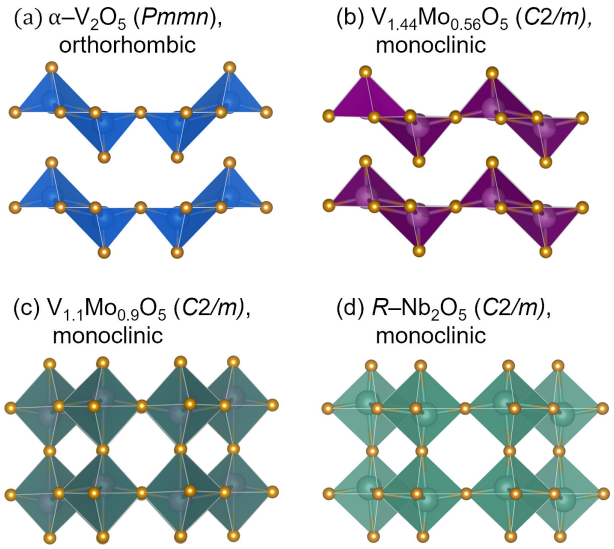

Figure 1: Reported crystal structures for $\alpha-V_2O_5$,[43] $V_{1.44}Mo_{0.56}O_5$,[44] $V_{1.1}Mo_{0.9}O_5$,[32] and $R-Nb_2O_5$.[12,37] These structures differ in the relative positions of transition metals, which in turn affects their coordination environments. The relative offset of transition metals from an octahedral coordination also varies; the relative direction of offsets in corner-sharing polyhedra are in the same direction in (a) $\alpha-V_2O_5$ and alternate directions in (b) $V_{1.44}Mo_{0.56}O_5$, (c) $V_{1.1}Mo_{0.9}O_5$, and (d) $R-Nb_2O_5$.

glycol and deionized (DI) water were combined in a 2:1 ratio by volume and stirred vigorously between 600 RPM and 700 RPM, at which homogeneous mixing was visually evident. Oxalic acid ($H_2C_2O_4{\cdot}2\,H_2O$) and ammonium metavanadate (NH_4VO_3) were added to the solution in a 2:1 molar ratio, allowing for each constituent to dissolve completely between additions. Finally, glacial acetic acid (CH_3COOH, anhydrous) was added in a ratio of 1:2 to the water in the initial solution. The precursor solution was 0.274 M of NH_4VO_3. For the Mo solution, oxalic acid, and ammonium molybdate tetrahydrate [$(NH_4)_6Mo_7O_{24}{\cdot}4\,H_2O$] were mixed vigorously in DI water in a 2:3 ratio by mass for 1 h, allowing for the complete dissolution of both constituents. The precursor solution was 0.006 M of $(NH_4)_6Mo_7O_{24}{\cdot}4H_2O$.

The V and Mo precursor solutions were combined (according to the target ratios) and stirred continuously for 12 h, during which the solution turned a dark yellow-green color. Solutions were transferred into a Teflon-lined autoclave where they were heated for 12 h, and then allowed to passively cool to room temperature. For compositions with $x = 0.05$, 0.1, 0.15, and 0.2, the autoclave set temperature was 200 °C; for compositions with $x = 0.4$, 0.6,

and 0.8, the autoclave set temperature was 190 °C.

Precipitates were washed and gathered from the solutions through repeated centrifugation and decanting with DI water and ethanol. The precipitate was then dried overnight at 70 °C and annealed in air at 500 °C. Compositions with $x = 0.05$, 0.1, 0.15, and 0.2 were annealed at 450 °C and compositions with $x = 0.4$, 0.6, and 0.8 were annealed at 500 °C. Furnaces were heated to the annealing temperatures at a rate of 4 °C per minute.

X-ray Diffraction

Powder XRD data, collected using a Panalytical X'Pert Powder Diffractometer, were used to screen hydrothermal and annealed samples in the $V_{2-x}Mo_xO_5$ series. High-resolution XRD data were acquired through the mail-in program at beamline 11-BM at the Advanced Photon Source (APS) at Argonne National Laboratory for as-prepared $V_{2-x}Mo_xO_5$ (with $x = 0.1$, 0.15, 0.2, 0.4, 0.6, and 0.8) and for lithiated $V_{1.95}Mo_{0.05}O_5$ and $V_{1.2}Mo_{0.8}O_5$. Quantitative analysis of diffraction data used GSAS-II.[45]

For synchrotron XRD, powders were loaded into 0.8 mm diameter Kapton capillaries sealed at both ends with epoxy. For lithiated samples, electrode powders (active material and conductive carbon additive) were collected from loose-powder Swagelok cells for *ex situ* XRD. In an Ar glovebox with no air-exposure, powders were washed with dimethyl carbonate (DMC) to remove any residual electrolyte salt, dried under vacuum, ground using an agate mortar and pestle, loaded into Kapton capillaries, and sealed with epoxy. Capillaries of cycled samples were sealed under Ar gas in secondary containers for shipping, with exposure of Kapton to air and moisture only at the beamline before measurements, thus mitigating potential changes to the material from the permeation of moisture through Kapton.

Visualizations of crystal structure data used VESTA.[46]

Cell Assembly and Cycling

Battery cycling was performed in home-built Swagelok cells (Fig. S1) with loose-powder composite electrodes of active material, $V_{2-x}Mo_xO_5$ (for x =0.05, 0.4, 0.6, 0.8), and SuperP conductive carbon additive (MSE Supplies) in an 8:2 ratio by mass, which were mixed using an agate mortar and pestle. Li metal served as both counter and reference electrode in these half-cells. Cathode and anode were separated by two Whatman glass filter dryer (GFD) separators and the electrolyte was a 1 M solution of $LiPF_6$ salt in ethylene carbonate (EC) and dimethyl carbonate (DMC) in a 1:1 ratio by volume (Aldrich).

Cells were assembled in an Ar glovebox and cycled galvanostatically at a rate of $C/10$ calculated for the theoretical reaction of 1 mol $V_{2-x}Mo_xO_5$ with 2 mol Li in 10 h, with potential limits of 1.5 V for discharge and 3.75 V for charge. Cells were cycled using a Bio-Logic VMP3.

Electron microscopy

Scanning electron microscopy (SEM) was performed using a TESCAN MIRA3 microscope with a beam voltage of 5 keV and a working distance of ≈15 mm. Samples were prepared on carbon tape and sputtered with a thin layer of gold to prevent charging.

Transmission electron microscopy (TEM) and scanning transmission electron microscopy (STEM) were performed using an FEI Talos F200X electron microscope (Thermo Scientific) at 200 keV. Samples for TEM were prepared by using a small scoop of starting material (concentration unknown) and adding 1000 μL of high purity distilled chloroform. The suspension was sonicated for 30 minutes in a water bath at room temperature and 10 μL of the suspension was dropcast onto a 200 mesh TEM Cu lacey grid (TedPella), followed by drying at 60 °C overnight.

Results and Discussion

Structural Evolution with Mo-substitution

High-resolution synchrotron XRD data show structural differences over the compositional series of the form $V_{2-x}Mo_xO_5$ for $x = 0.1$, 0.15, 0.2, 0.4, 0.6, and 0.8 (Fig. 2). Overall, the changes in peak positions and intensities are consistent with our expectations for partial substitution of V^{5+} by larger Mo^{6+}. Generally, changes in peak positions reflect a decrease in the c lattice parameter (the layer stacking direction) and an increase in the a lattice parameter (Fig. 1a). Previous work shows that substitution by Mo^{6+} also results in some reduction of V from the 5+ to 4+ oxidation state.[32,47] The larger radii of Mo^{6+} and V^{4+} are associated with a shift from square pyramidal toward octahedral-like coordination of the transition metals.[35] This change in coordination drives the decrease in interplanar distance (c parameter), such that the long M–O bond across layers decreases. In addition, impurities are evident for several compositions, which are discussed with quantitative results of Rietveld refinements.

Bragg peaks in XRD data over the series are best captured by three atomic structure models, depending on x: orthorhombic $\alpha-V_2O_5$ ($Pmmn$)[43] for $x \leq 0.2$ (Fig. 1a), monoclinic $V_{1.44}Mo_{0.56}O_5$ ($C2/m$)[44] for $x = 0.4$ (Fig. 1b), and monoclinic $V_{1.1}Mo_{0.9}O_5$ ($C2/m$)[32] for $x = 0.6$ (Fig. 1c). The primary distinction of these structures is the lattice parameter associated with their layer stacking direction, c, which decreases with increasing Mo content. In addition, these structures are different in the relative positions of cations in corner- and edge-sharing square pyramids. In $\alpha-V_2O_5$, pairs of transition metals in corner-sharing square pyramids are displaced away from an octahedral center in the same direction (Fig. 1a). In published structures with Mo content $x \geq 0.56$, transition metals in corner-sharing square pyramids are displaced away from an octahedral center in opposite directions, with the offset from an octahedral center alternating higher and lower (Fig. 1b and c).[18]

At low Mo concentrations ($x = 0.1$, 0.15, 0.2), d-spacings associated with the (200), (110),

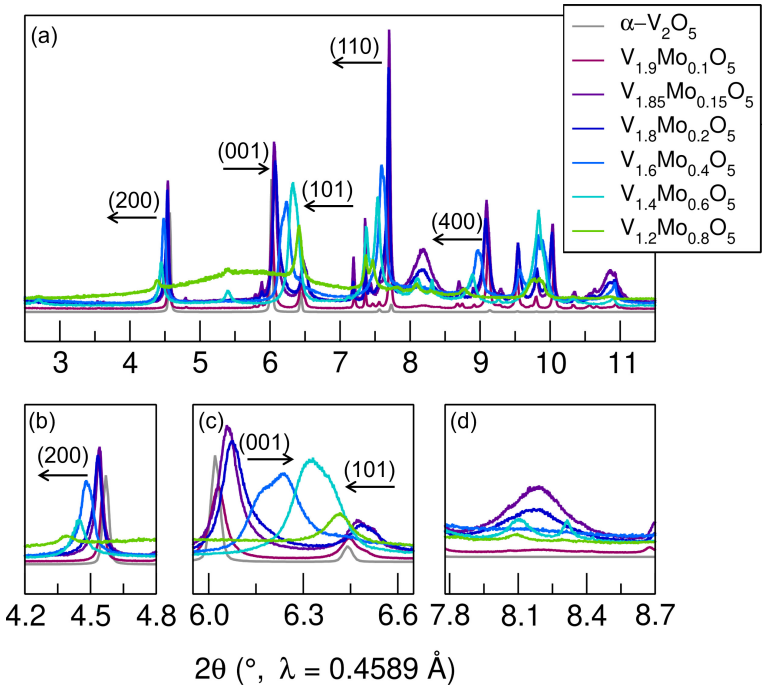

Figure 2: (a) High-resolution synchrotron XRD data for the series $V_{2-x}Mo_xO_5$ in the range from $0.1 \leq x \leq 0.8$ and simulated XRD data for $\alpha-V_2O_5$. Mo-substitution results in shifts in the positions of several reflections, including (b) the (200) and (c) the (110) peaks. (d) Peaks near 8.25° correspond to impurity phase(s) and vary with Mo content.

and (400) planes of $\alpha-V_2O_5$ ($Pmmn$) increase with increasing Mo content, indicated by the shifts of these reflections to lower 2θ positions (Fig. 2a and b). Two peaks near 6.0° and 6.5° correspond to the (001) and (101) reflections in V_2O_5 (Fig. 2c). The (001) reflection shifts to higher 2θ over the series, consistent with the expected decrease of the c parameter and interlayer spacing with increasing Mo substitution (Fig. 2c). The trends we find in this compositional range are overall consistent with recent work by Schofield *et al.* in a similar concentration of Mo-substitution in V_2O_5.[27]

For $x \geq 0.4$, the (001) and (101) reflections shift closer together, toward a single reflection (Fig. 2c), due to the (101) reflection being disallowed for the monoclinic structures, $V_{1.44}Mo_{0.56}O_5$ and $V_{1.1}Mo_{0.9}O_5$. This trend toward a single peak is associated with a shift of transition metal positions, specifically, the change from transition metals in corner-sharing polyhedra being offset from an octahedral position in the same direction in V_2O_5 to alternating directions with Mo substitution (Fig. 1a, b, and c).[44] The resulting transition metal posi-

tions are similar to those in $R{-}Nb_2O_5$, which has an idealized V_2O_5 structure (Fig. 1d).[12,37] The (100) reflection of $R{-}Nb_2O_5$ ($A2/m$), corresponding to the layer stacking direction, is similar to the merging (001) and (101) peaks near 6.5° for samples with $x \geq 0.4$.[12,37,44]

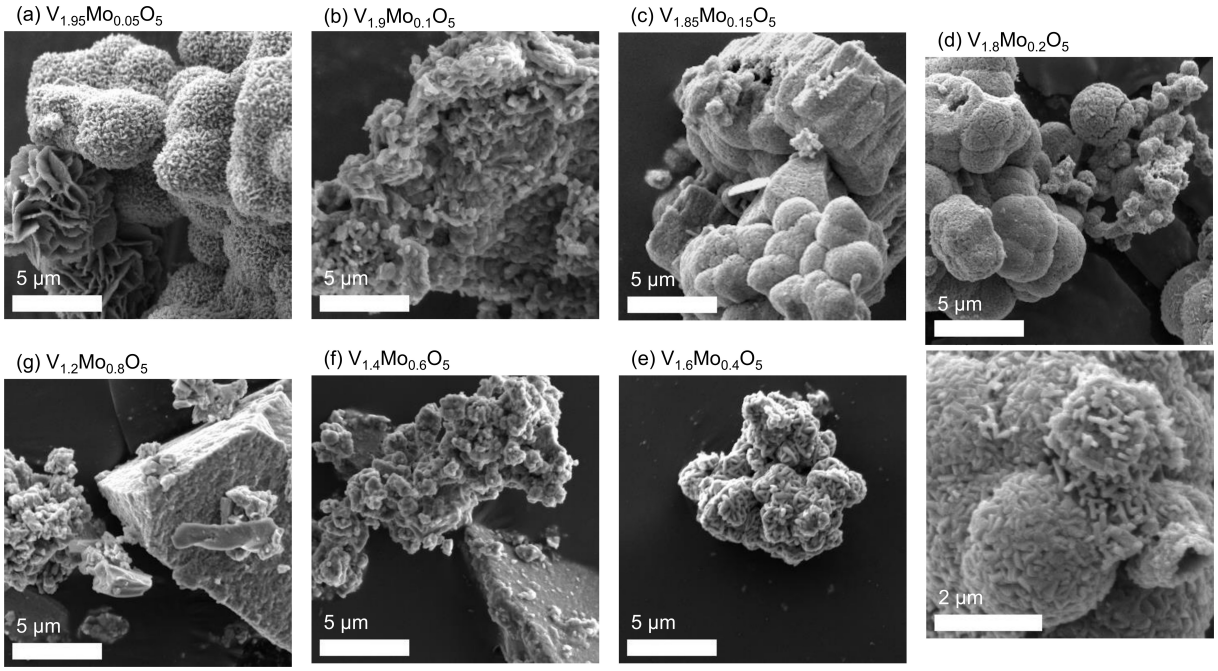

Figure 3: Irregular particles with no systematic variation are observed by SEM for $V_{2-x}Mo_xO_5$ with $x = 0.05$, 0.1, 0.15, 0.2, 0.4, 0.6, and 0.8.

In addition to changes of peak positions, increasing Mo content also results in changes to peak shape, specifically peak broadening (Fig. 2). The changes in peak shape are especially extreme for the (200) and (110) reflections for compositions with $x \geq 0.4$, even with high-resolution synchrotron XRD data (Fig. 2b and c). SEM images show that there is not a systematic change in the size of primary or agglomerated particles with Mo content (Fig. 3).

TEM images aid with the interpretation of XRD data, especially possible origins of the large residuals of Rietveld fitting and peak shapes. TEM micrographs of $V_{1.6}Mo_{0.4}O_5$ show polycrystalline domains on the order of tens of nanometers (Fig. 4a and b). The fast Fourier transform (FFT) of the high-resolution image shows the [100] zone axis (Fig 4c). At higher magnification, micrographs and inverse FFT (IFFT) images show lattice fringes associated with the crystallographic shear planes in several domains (Fig. 4e and f). In the lower left of

the high-magnification images, a grain boundary between regions with different orientations are visible. In the upper right-hand side of the images, there is evidence of misalignment through the depth of the sample, such as has been seen in micrographs from oxides with crystallographic shear planes due to twins, stacking faults, and other extended defects.[48–50] The relatively subtle nature of defects in $V_{1.6}Mo_{0.4}O_5$ is consistent with the better Rietveld fit for this compound relative to other compositions. The residuals that are present for this compound can be explained by the misalignments and other defects apparent in the TEM data.

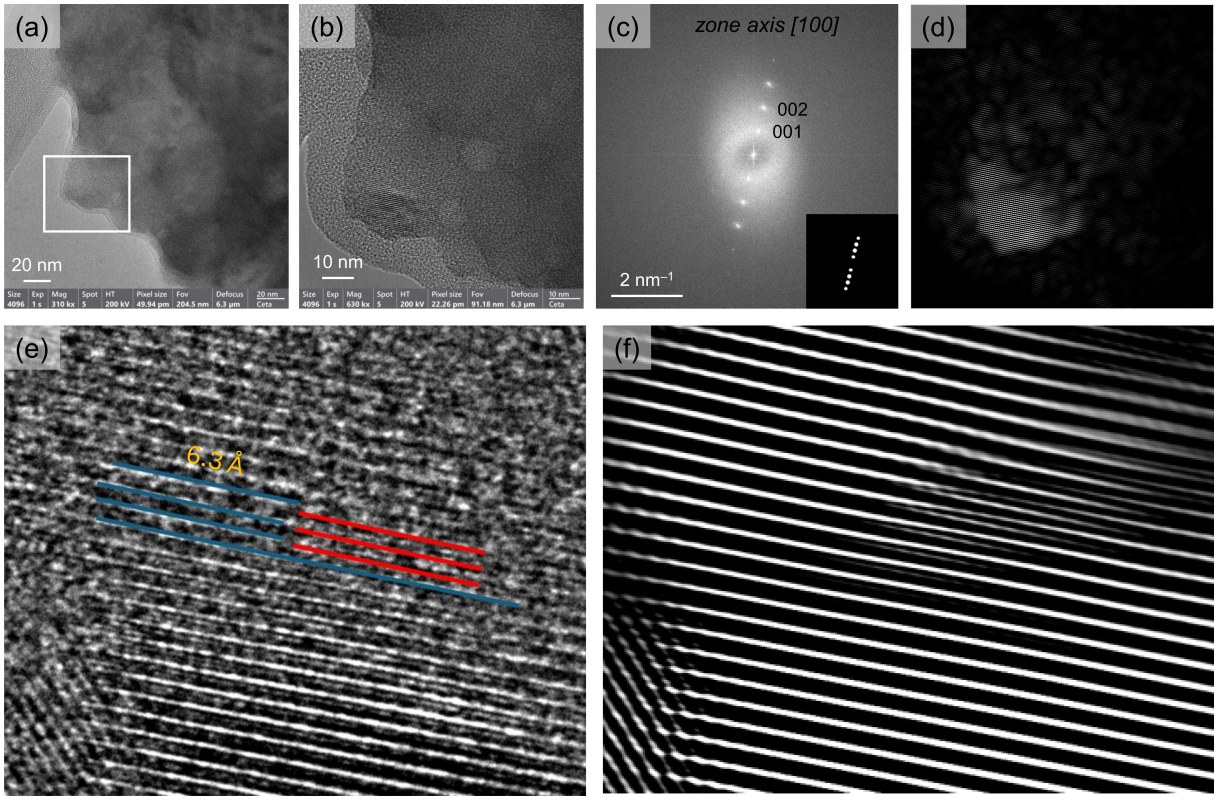

Figure 4: (a) Low and (b) high-resolution TEM images of $V_{1.6}Mo_{0.4}O_5$. (c) The resulting FFT from the high-resolution TEM image (b) shows the [100] zone axis and (d) its correlating mask to calculate the IFFT. (e) A higher magnification of area (b) shows lattice fringes that correspond to (f) a magnified area of the IFFT, allowing visualization of lattice fringes as well as their disruptions due to grain boundaries and defects.

Likewise, TEM images aid the interpretation of XRD data for $V_{1.2}Mo_{0.8}O_5$. TEM images show much smaller crystalline domains for this composition (< 10 nm, Fig 5a and b), which

contribute to the broadening of XRD peaks. The nanocrystalline domains are separated by disordered regions, which result in to the large background feature in XRD data. In contrast to $V_{1.6}Mo_{0.4}O_5$, the combination of smaller domains with larger distribution of orientations as well as disordered regions result in a variety of features in high-magnification and IFFT images for $V_{1.2}Mo_{0.8}O_5$. Other features include wobbly lamellar features as well as disruptions of lamellar features, such as intergrowths (highlighted in red ovals, Fig 5e and f). These disruptions to periodicity explain the high residuals of Rietveld fits for $V_{1.2}Mo_{0.8}O_5$.

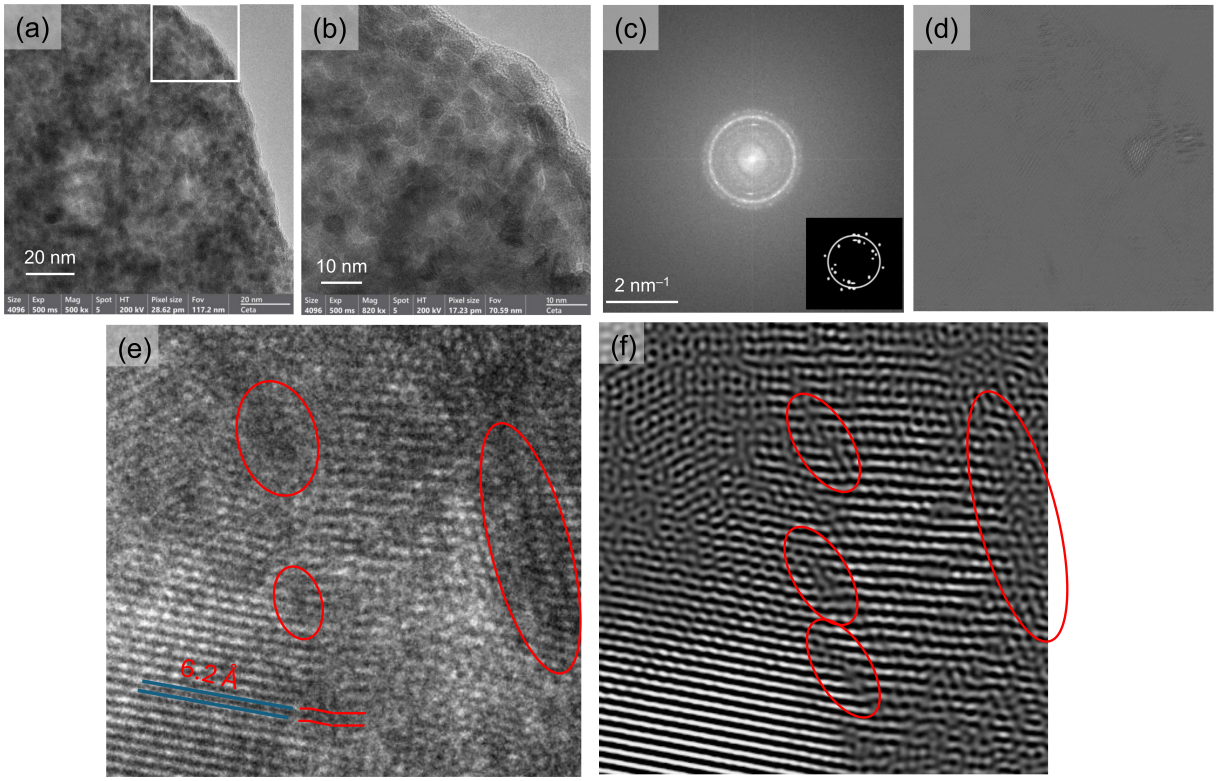

Figure 5: (a) Low and (b) high-resolution TEM micrographs of $V_{1.2}Mo_{0.8}O_5$ show nanocrystalline domains separated by disordered regions. (c) FFT of the high-resolution TEM image highlights the nanocrystalline nature of the sample and (d) its correlating mask to calculate the IFFT. (e) A higher magnification of area (b) shows lattice fringes that correspond to (f) a magnified area of the IFFT, allowing visualization of regions with ordered lattice fringes and regions with disorder, such as intergrowths indicated by red ovals.

Synchrotron XRD data also reveal impurity peaks for most compositions (Fig. 2). Peaks at 2.7° and 5.4° correspond to $V_{3.6}Mo_{2.4}O_{16}$, which has three-polyhedra-wide slabs of corner-sharing polyhedra, connected by edge-sharing polyhedra at crystallographic shear planes

(Fig. S2b). This composition is sometimes referred to as V_2MoO_8 or $V_9Mo_6O_{40}$, which have been reported with the same structure type and slight differences in composition.[51–53] In some samples, we also see peaks associated with the V_2MoO_8-type impurity between 8.0° and 8.5° (Fig. 2d). For $x = 0.6$ and 0.8, the impurity phase contributes two sharp peaks, which correspond to the (600) and (401) planes (Fig. S3). For $x = 0.15$ and 0.20, a single broad peak is centered in this 2θ region. While much lower intensity, there is a broad feature in this range for $x = 0.1$ and 0.4. A V_2MoO_8-type impurity was also observed by Schofield *et al.*, who reported an increase in the phase fraction of this impurity with increasing Mo content in their $V_{2-x}Mo_xO_5$ series for $0.106 \leq x \leq 0.166$.[27,30,44]

Several other impurity peaks are observed for $V_{2-x}Mo_xO_5$ with $x = 0.1$, 0.15, and 0.2, such as at 5.5° and 11.5°. We are not able to identify a specific phase to which these peaks can be attributed, suggesting a mixture of other impurity phases are present. These secondary impurities are not present for higher Mo content samples, specifically those with $x \geq 0.4$, for which a V_2MoO_8-type phase is the only impurity (Fig. S3b).

To better understand the atomic structure changes associated with Mo substitution, synchrotron XRD data were quantitatively analyzed using Rietveld refinement. The structural models used for refinements varied with Mo content, based on our qualitative analyses. We discuss refinements of three compositions in detail, specifically $V_{1.9}Mo_{0.1}O_5$, $V_{1.6}Mo_{0.4}O_5$, and $V_{1.4}Mo_{0.6}O_5$ (Fig. 6). Refinements for other compositions are provided in the SI (Fig. S4, S5, and S6).

In starting models, the V and Mo mixed occupancies of transition metal sites reflected the target composition (Table S1). V and Mo occupancies were fixed and the position and U_{iso} of the transition metal crystallographic site were constrained to be equivalent. Additional details regarding the starting models and refined parameters are provided in the SI (Tables S1 through S7). Due to the presence of varying amounts of impurities for most compositions, including unidentified impurities, secondary phases were not included in the refinement models. As such, fits have relatively high residuals, but nonetheless support our

understanding of structural changes driven by Mo-substitution in V_2O_5.

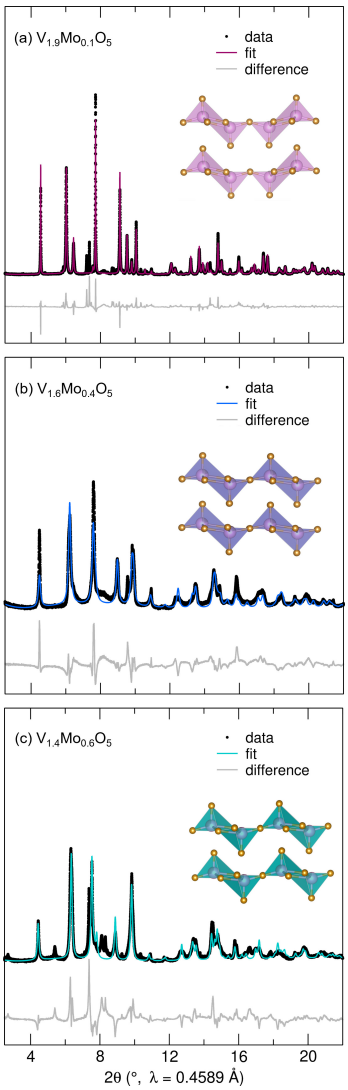

Figure 6: Rietveld refinements of synchrotron XRD data for (a) $V_{1.9}Mo_{0.1}O_5$, (b) $V_{1.6}Mo_{0.4}O_5$, and (c) $V_{1.4}Mo_{0.6}O_5$ capture the primary reflections well. For some, higher differences result from impurities, peak intensity mismatch, peak shape mismatch, or combinations thereof. Refined atomic structure models illustrate the shift in transition metal position with increasing Mo content.

For $V_{1.9}Mo_{0.1}O_5$, the starting model for Rietveld refinement was based on $\alpha-V_2O_5$, modified to have mixed occupancy of V and Mo on the cation site.[43] Consistent with peak shifts described qualitatively above (Fig. 2), refined lattice parameters indicated an increase of a and a decrease of c relative to the starting model (Table S2). For compositions with $x = 0.15$ and 0.2 (Fig. S4 and S4), a and c further increase and decrease, respectively, as x

increases (Tables S3 and S4).

The presence of impurity phases are highlighted by regions of mismatch between the measured data and the calculated fits. For example, the broad peak at 8.2° in the $V_{1.9}Mo_{0.1}O_5$ XRD data increases in intensity with increasing x in lower Mo content compositions ($x = 0.1$, 0.15, 0.20) and can be attributed to the (600) reflection of the main V_2MoO_8-type impurity (Fig. 2d and S2a). This reflection is associated with the three-polyhedra wide slabs of the V_2MoO_8 structure type.[51,52] The breadth of this feature possibly indicates intergrowths of three-polyhedra wide slabs among the two-polyhedra-wide slabs of the parent V_2O_5 structure, similar to 'Wadsley intergrowth defects' reported by Moore *et.al.* in Wadsley−Roth phases.[54] The progressive increase in the intensity of this broad reflection with increasing Mo content (for $x = 0.1$, 0.15, and 0.2) suggests that the occurrence of intergrowths increases with increasing Mo content, reflecting the limited solubility of Mo in V_2O_5.[27,55]

Fits for low Mo content compositions ($x = 0.1$, 0.15, 0.20) have a peak intensity mismatch to at 7.7°, with a larger mismatch for $V_{1.85}Mo_{0.15}O_5$ and $V_{1.8}Mo_{0.2}O_5$ (Fig. S4 and S5). Fits for $V_{1.85}Mo_{0.15}O_5$ and $V_{1.8}Mo_{0.2}O_5$ also have a larger mismatch in intensities than $V_{1.9}Mo_{0.1}O_5$ for peaks at ≈11° and 16°, which correspond to the (401) and (021) reflections of the orthorhombic $\alpha-V_2O_5$ structure. From these X-ray data, we are not able to distinguish whether the mismatches are related to O positions, cation ordering, impurity phase(s), or combinations thereof.

The presence of overlapping impurity peaks and peak intensity mismatch contribute to fits with high residuals for $V_{1.9}Mo_{0.1}O_5$ ($R_{wp} = 19.7\%$), $V_{1.85}Mo_{0.15}O_5$ ($R_{wp} = 30.2\%$), and $V_{1.8}Mo_{0.2}O_5$ ($R_{wp} = 26.6\%$). Even so, the primary peaks are captured using the orthorhombic model, in which transition metal offsets are in the same direction in corner-sharing polyhedra, rather than in opposite directions as in the monoclinic polymorphs reported for higher Mo content $V_{2-x}Mo_xO_5$.[32] Overall this indicates that Mo-substitution of $x \leq 0.2$ is insufficient to initiate substantial changes in the V_2O_5 framework.[18,27]

For $V_{1.6}Mo_{0.4}O_5$, XRD data are fit using a structure based on monoclinic $V_{1.44}Mo_{0.56}O_5$

($C2/m$, Fig. 1b).[44] Using this structural model, peak positions are captured well, despite some intensity mismatch (Fig. 6b). $V_{1.6}Mo_{0.4}O_5$ has the smallest fraction of secondary phases relative to the other compositions we evaluated, but still a moderate mismatch ($R_{wp} = 21.7\%$). While the broad peak near 8°, associated with the three-polyhedra-wide slabs of V_2MoO_8, is present, the breadth and low intensity of the feature indicate a lower occurrence of three-polyhedra-wide intergrowths at this composition.

The reported structure of $V_{1.1}Mo_{0.9}O_5$ ($C2/m$, Fig. 1c)[32] was refined against XRD data for $V_{1.4}Mo_{0.6}O_5$ (Fig. 6c). The fit shows good agreement with peak positions and some mismatch in peak intensity. The primary impurity for $V_{1.4}Mo_{0.6}O_5$ is V_2MoO_8, which contributes to uncaptured peaks in the range $5° < 2\theta < 10°$ (Fig. S3b) and an $R_{wp} = 25.9\%$.

For the composition with the highest Mo content, $V_{1.2}Mo_{0.8}O_5$, the starting model for the refinement was based on the structure refined against the $V_{1.6}Mo_{0.4}O_5$ data. The refinement captures the data well, with some impurity peaks in the range $5° < 2\theta < 10°$ (Fig. S3b and 2b), which correspond to the primary V_2MoO_8-type impurity. The diffraction data for this composition show extensive diffuse scattering, manifesting as a broad feature centered at 5°, which suggests a high degree of disorder, including amorphous regions.

For compositions with $x \geq 0.4$, the refined lattice parameters evolve smoothly with an increase in a and decrease in c, producing similar residuals for fits: 21.7% for $V_{1.6}Mo_{0.4}O_5$, 25.9% for $V_{1.4}Mo_{0.6}O_5$, and 13.02% for $V_{1.2}Mo_{0.8}O_5$ (Tables S5, S6, and S7). We emphasize the trend of behavior, more than absolute values, as the actual composition of $V_{2-x}Mo_xO_5$ phases differ from the targets due to the presence of impurity phases. Further, the impurity phases can have a range of compositions, which prevent deriving accurate relationships of sample composition and lattice parameters. However, we note the similarities between our and previously reported lattice parameters.[12,32,43,44]

The values of the stacking direction lattice parameter lie between those previously reported for the analogous features in V_2O_5 and $R-Nb_2O_5$ (Fig. 7). This trend indicates a progressive change of the structure from the true $\alpha-V_2O_5$ structure towards that of idealized

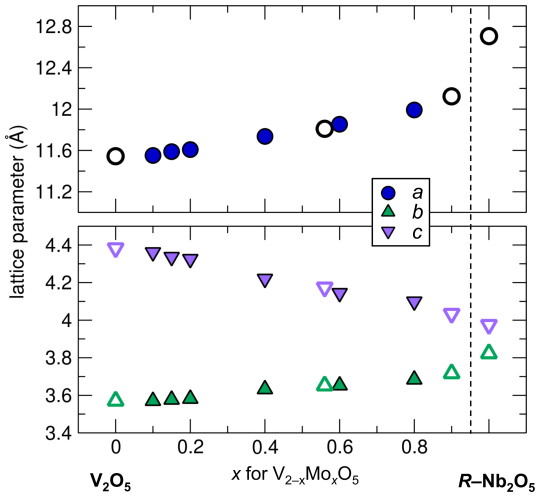

Figure 7: Lattice parameters (a, b, and c) vary with Mo content in the series $V_{2-x}Mo_xO_5$ for $0.1 \leq x \leq 0.8$. Notably, lattice parameters for the Mo-substituted series fall between those of $\alpha-V_2O_5$ and $R-Nb_2O_5$. Lattice parameters for this work are represented by filled symbols, while open symbols represent lattice parameters from previously reported structures for V_2O_5,[43] $V_{1.44}Mo_{0.56}O_5$,[44] $V_{1.1}Mo_{0.9}O_5$,[32] and $R-Nb_2O_5$.[12]

V_2O_5, for which $R-Nb_2O_5$ is the closest realized material.[37] This progression has been previously observed in individual compositions in the $V_{2-x}Mo_xO_5$ system.[24,32,36] The structural variation with composition indicates that as Mo^{6+} content increases, a greater portion of V^{5+} must be reduced to V^{4+} to maintain charge neutrality.[8,24] As a result, the larger radii of V^{4+} and Mo^{6+} in six-fold coordination environments (0.58 Å and 0.59 Å, respectively) compared to V^{5+} (0.54 Å) drives the structure towards an octahedral-like coordination.[16,35,56] However, the ionic radii are still smaller than Nb^{5+} (0.64 Å), and impurity phases preferentially form at higher Mo concentrations, thus the idealization of the V_2O_5 structure through substitution of V by Mo is limited relative to $R-Nb_2O_5$.

Battery Cycling

Upon lithiation, $\alpha-V_2O_5$ undergoes multiple phase transformations, including to form ϵ, δ, and γ polymorphs, which are reflected in cycling data as a series of plateaus and sloped regions corresponding to phase transformations and solid solution reactions, respectively.[13,15,30,57,58] When discharged to potentials below 1.9 V, there is also a transformation to the ω polymorph,

which is a disordered rocksalt oxide with the formula $Li_yV_2O_5$.[8,15,23,24] In following cycles to low potentials, there are two proposed charge storage mechanisms. One is a solid solution mechanism in the ω polymorph for $0.2 \leq y \leq 3$;[15] another is a two-phase transformation between ω and β polymorphs of lithiated V_2O_5.[23]

Based on changes in atomic structure from $\alpha-V_2O_5$ toward its three-dimensionally-connected idealized structure, we anticipated the nature of phase transformations during cycling would likewise differ with Mo content. While we do not in any case see cycling data similar to that of $R-Nb_2O_5$,[12] there are changes in the series of phase transformation on the first discharge with Mo content (Fig. 8). We see changes in cycling profiles in the first discharge as well as in later cycling, driven by the chemical and structural changes associated with Mo substitution. Especially, we see decreased hysteresis and improved capacity retention for higher Mo content compositions.

We discuss cycling behavior for $V_{2-x}Mo_xO_5$ compositions with $x = 0.05$, 0.4, 0.6, and 0.8. Materials were cycled in loose-powder Swagelok cells at a cycling rate of $C/10$, such that 2 moles of Li react per mole of $V_{2-x}Mo_xO_5$ in 10 h (Fig. 8 and 9).

The features in galvanostatic cycling indicate that the lithiation of the lowest Mo content composition, $V_{1.95}Mo_{0.05}O_5$, follows a similar series of two-phase transformations as $\alpha-V_2O_5$,[15,24,27] specifically, near voltages of 3.25 V, 2.4 V, and 2 V (Fig. 8a). The positions of plateaus are especially evident when these cycling data are plotted as differential capacity (Fig. 9a). After the first discharge, delithiation and lithiation occur through solid solution-type reactions, indicated by the relatively smooth profiles in galvanostatic cycling (Fig. 8a), which are evident in the differential capacity plot as single broad features centered around $\approx$2.5 V (Fig. 9a). During the first cycle, there is an irreversible capacity corresponding to $\approx$0.5 moles of Li per formula unit of active material. Following the first cycle, cycling profiles are similar to those reported for $\alpha-V_2O_5$ to voltages below 1.9 V, as smooth profiles (Fig. 8a).[15,23] Over 15 cycles, $V_{1.95}Mo_{0.05}O_5$ retains only $\approx$65% capacity (Fig. 8a).

Schofield *et al.* have previously reported the series of phase transformations during

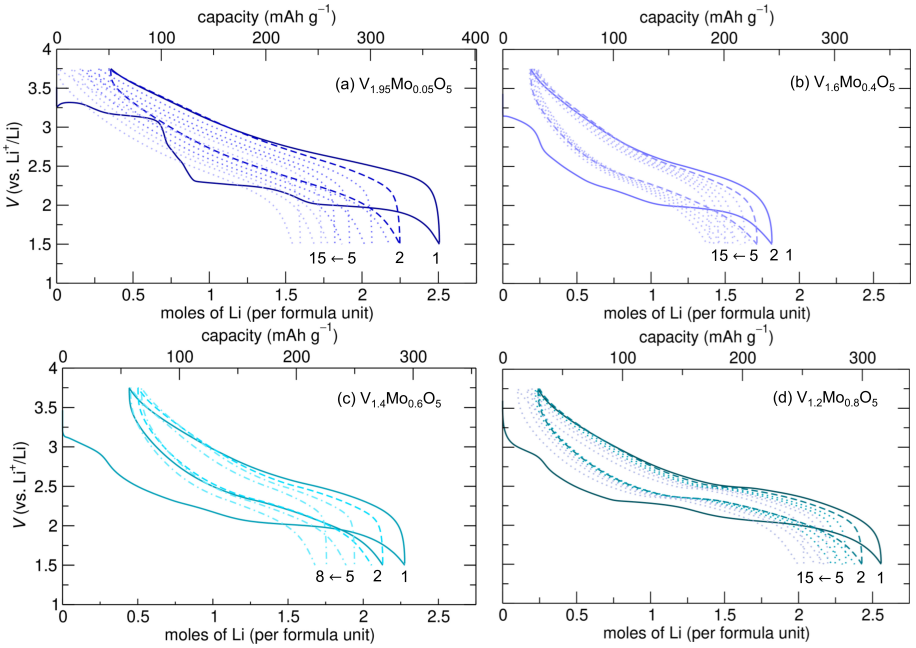

Figure 8: Galvanostatic cycling for loose-powder Swagelok cells cycled at a rate of $C/10$ between 1.5 V and 3.75 V for (a) $V_{1.95}Mo_{0.05}O_5$, (b) $V_{1.6}Mo_{0.4}O_5$, (c) $V_{1.4}Mo_{0.6}O_5$, and (d) $V_{1.2}Mo_{0.8}O_5$.

lithiation of $V_{2-x}Mo_xO_5$ for $x < 0.2$.[27] Using *operando* XRD, they find that rather than the progression from α to ϵ to δ to γ, with Mo substitution there is a co-existence of phases ϵ', δ, and γ. When we compare their reported cycling data to our galvanostatic cycling profiles for $x \geq 0.4$, we see fewer features at high potentials, suggesting a different series of two-phase transformations.

Lithium insertion in compositions with higher Mo content, *i.e.*, $V_{2-x}Mo_xO_5$ with $x = 0.4$, 0.6, and 0.8, have more pronounced differences from $\alpha-V_2O_5$ in their first discharge profiles (Fig. 8). The abrupt and pronounced plateaus in $\alpha-V_2O_5$ and $V_{1.95}Mo_{0.05}O_5$ are smoothed for $V_{1.6}Mo_{0.4}O_5$, $V_{1.4}Mo_{0.6}O_5$, and $V_{1.2}Mo_{0.8}O_5$. In addition, less capacity is attributed to the two-phase transformations at high potentials. This could reflect what Schofield *et al.* identified as 'pre-transformation' induced by Mo-substitution, which was supported by their *operando* XRD analysis.[27] The changes we see in the first discharge profile with Mo content are further evident when galvanostatic cycling data are plotted as differential capacity, especially the smoothing of high potential plateaus (Fig. 9).

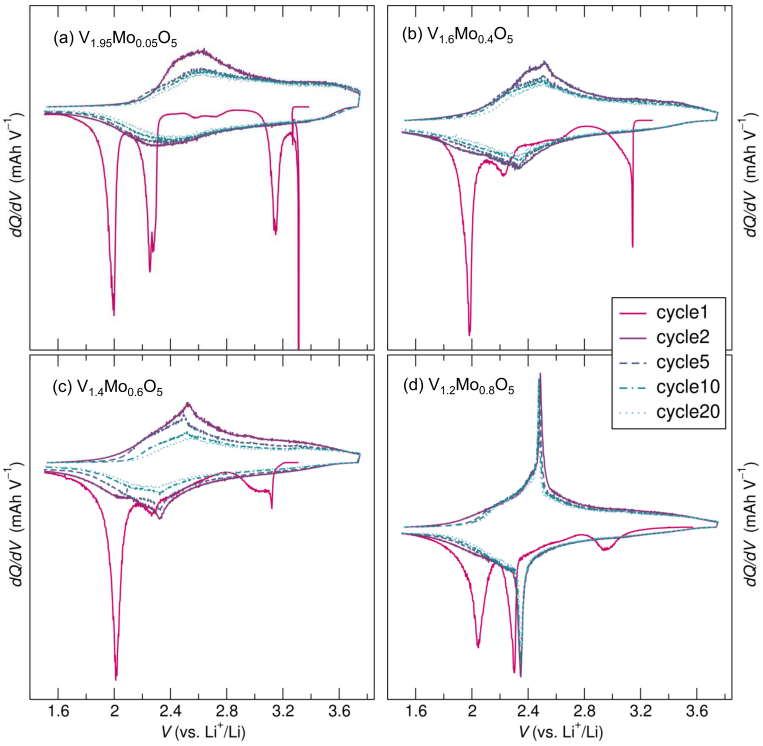

Figure 9: Differential capacity plots highlight two-phase and solid solution reactions during the galvanostatic cycling of (a) $V_{1.95}Mo_{0.05}O_5$, (b)$V_{1.6}Mo_{0.4}O_5$, (c)$V_{1.4}Mo_{0.6}O_5$, and (d)$V_{1.2}Mo_{0.8}O_5$.

We attribute theses cycling profile changes to atomic structure changes driven by Mo substitution in V_2O_5. While our XRD data show the compositional series has a variety of types and amounts of impurity phases, such as V_2MoO_8, the high potential region of cycling data for V_2MoO_8 has different features than in the compositional series we report here.[53]

That Mo substitution, rather than the presence of impurities, drives these changes in cycling behavior is further supported by similar changes in first discharge cycling profiles when other transition metals are used to modify V_2O_5, such as Al^{3+} and Mn^{2+}.[14,28]

The cycling profiles for the first charge and subsequent cycles of $V_{1.6}Mo_{0.4}O_5$, $V_{1.4}Mo_{0.6}O_5$, and $V_{1.2}Mo_{0.8}O_5$ are unique from those of their first discharges (Fig. 8 and 9). Comparing the shapes of differential capacity plots of the first charge and later cycles, we see that the smooth, broad shapes of the first charge and later cycling with low Mo content develop into sharper features with increasing Mo content (Fig. 9). The most pronounced change in cycling features appear as short plateaus in cycling profiles (Fig. 8d) and as a defined peak in differential capacity (Fig. 9d) for $V_{1.2}Mo_{0.8}O_5$. Cycling data for $V_{1.2}Mo_{0.8}O_5$ are also distinct from other compositions in the decreased hysteresis between discharge and charge curves in the second and later cycles.

The differences in the as-prepared materials and first discharge products contribute to differences in cycling profile shapes, as well as differences in cycling performance. Even in unoptimized cells as loose powders, compared to the 65% capacity retention of $V_{1.95}Mo_{0.05}O_5$ in the first 15 cycles, capacity retention is improved in higher Mo content compositions. For $V_{1.6}Mo_{0.4}O_5$ and $V_{1.4}Mo_{0.6}O_5$, 74% and 73% of the first discharge capacities are retained at the 15^{th} and 8^{th} cycles, respectively. Power interruption during cycling disrupted the acquisition data to later cycles for $V_{1.4}Mo_{0.6}O_5$. For $V_{1.2}Mo_{0.8}O_5$, we see 78% capacity retention in the first 15 cycles.

The change in performance indicates differences in the phases that form at the end of the first discharge as a function of initial composition and structure. The different first discharge products likewise have differences in their lithiation and delithiation mechanisms. Toward

understanding the differences in the later cycling behavior, we collected *ex situ* synchrotron XRD data on discharged powders for $V_{1.95}Mo_{0.05}O_5$ and $V_{1.2}Mo_{0.8}O_5$. These data were compared to XRD data of pristine $V_{1.9}Mo_{0.1}O_5$ and $V_{1.2}Mo_{0.8}O_5$, as well as to reported data for $R-Nb_2O_5$ and its discharge product (Fig. 10).[12] Data show that the discharge product of $V_{1.95}Mo_{0.05}O_5$ is crystalline, but its peaks cannot be indexed to known phases comprising Li, V, Mo, and O (Fig. 10a).

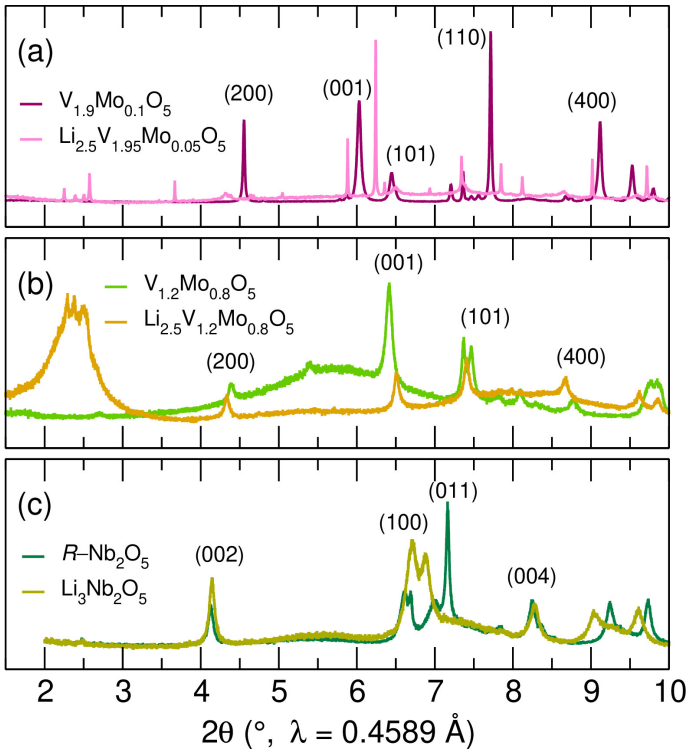

Figure 10: Synchrotron XRD data of pristine and lithiated first discharge products for (a) $V_{1.95}Mo_{0.05}O_5$, (b) $V_{1.2}Mo_{0.8}O_5$, and (c) $R-Nb_2O_5$ (adapted from reference[12]). For (a) $V_{1.95}Mo_{0.05}O_5$, it is difficult to relate reflections between the initial and lithiated structures. For (b) $V_{1.2}Mo_{0.8}O_5$, there are relationships between the (200), (001), (001), and (400) reflections in the initial and lithiated structures. The shifts are reminiscent of the structural changes of the (002), (100), (011), and (004) reflections in (c) $R-Nb_2O_5$.

For $V_{1.2}Mo_{0.8}O_5$, we also find the lithiation product has several reflections (Fig. 10b). Many of these appear in similar locations as the prepared material, but there is also a large diffuse feature at low 2θ that cannot be readily assigned to a specific origin. The large diffuse feature does, however, suggest disorder in the discharge product, perhaps related to similar features in disordered rocksalt structures in which short-range ordering gives rise to

diffuse features at low angles.[8,36,59] Ambiguity of the discharge product likewise prevents the determination of the precise cycling mechanism in later cycles.

Regardless, the cycling and structural data we report for $V_{1.2}Mo_{0.8}O_5$ prepared by solvothermal methods show a unique charge storage mechanism relative to lower Mo substitution compounds,[27] Mo-substituted V_2O_5 prepared by solid state methods,[24,30] V-Mo-O bronzes,[36] and materials with V_2MoO_8-type structures and similar V:Mo ratios, such as $V_9Mo_6O_{40}$.[53,60] We believe the difference in cycling profiles and behavior result from differences in the cation distribution or local coordination environments in the ω-like structure that forms during the first discharge, which appears to vary with Mo content.

Conclusions

Using synchrotron XRD and Rietveld refinement, we find changes in atomic structure with composition over the series $V_{2-x}Mo_xO_5$, wherein $0.05 \leq x \leq 0.8$. Structural changes with increasing Mo content include a shift of transition metal coordination from square pyramidal toward octahedral, which is expected based on the relative radii and preferred coordination of V and Mo. Associated with this coordination change is a contraction of the c lattice parameter, which is in the layer stacking direction. This decrease in c approaches the structure of $R-Nb_2O_5$, which is considered an 'idealized' $\alpha-V_2O_5$. Hence, a structural progression towards $R-Nb_2O_5$-like connectivity is observed with $x \geq 0.4$, yet idealization with Mo substitution is not realized. This is likely due to thermodynamic instability of the Mo-substituted structures, such that secondary phases and planar defects (*e.g.*, Wadsley intergrowths) form with increasing Mo content.

The structural changes that result from Mo substitution are not sufficient to change the lithiation behavior to resemble that of $R-Nb_2O_5$, which undergoes only minor structural changes during Li intercalation and deintercalation. Instead, Mo-substituted samples still undergo a series of two-phase transformations during their first discharge, followed by distinct

reactions in following cycling. The profile shapes of later cycles vary with Mo content, driven by differences in the composition and structure of the discharge products. The mechanistic differences affect cycling performance, with better capacity retention and lower hysteresis in $V_{1.2}Mo_{0.8}O_5$ than in samples with lower Mo content.

While we are not able to precisely determine the differences in discharge products or cycling mechanisms in later cycles as a function of Mo content, our results indicate that the cycling behavior of V_2O_5 to deep discharge can be improved with high rates of Mo-substitution. Our data suggest opportunities to modify the electrochemical energy storage of V_2O_5, and is relevant to other disordered rocksalt oxide electrode materials.

Acknowledgements

B.G.G. acknowledges support through the Summer Undergraduate Research experience at the University of Florida in the Herbert Wertheim College of Engineering. KAP and BSG would like to thank the U.S. Department of Energy, Office of Science, Office of Basic Energy Sciences under Award Number DE-SC-0024346 for partial salary support. This research made use of the Research Services Center at the University of Florida. This research made use of several beamline facilities at national laboratories. Use of the Advanced Photon Source (APS) at Argonne National Laboratory was supported by the U. S. Department of Energy, Office of Science, Office of Basic Energy Sciences, under Contract No. DE-AC02-06CH11357. This research used the mail-in program at beamline 11-BM of the APS. We also acknowledge support by beamline scientists and staff at this facility, especially Saul Lapidus. This work was supported by an NSF EAGER award under award number DMR 2334240.

References

(1) Armand, M.; Tarascon, J.-M. Building better batteries. *Nature* **2008**, *451*, 652–657.

(2) Althaf, S.; Babbitt, C. *Critical Materials and Sustainability Transition*; CRC Press, 2023; pp 34–51.

(3) Dunn, B.; Kamath, H.; Tarascon, J. M. Electrical energy storage for the grid: A battery of choices. *Science* **2011**, *334*, 928–935.

(4) Booth, S. G. et al. Perspectives for next generation lithium-ion battery cathode materials. *APL Materials* **2021**, *9*, 109201.

(5) Clément, R.; Lun, Z.; Ceder, G. Cation-disordered rocksalt transition metal oxides and oxyfluorides for high energy lithium-ion cathodes. *Energy Environ. Sci.* **2020**, *13*, 345–373.

(6) Yu, X.; Manthiram, A. Sustainable battery materials for next-generation electrical energy storage. *Adv. Energy Sustainability Res.* **2021**, *2*, 2000102.

(7) Saber, M.; Van der Ven, A. Redox Mechanisms upon the Lithiation of Wadsley–Roth Phases. *Inorg. Chem.* **2024**, *63*, 11041–11052.

(8) Leesmith, M. J.; Halcovitch, N. R.; Hua, X. Electrochemical lithiation-induced formation of disordered rocksalt. *J. Mater. Chem. A* **2023**, *11*, 17027–17034.

(9) Cava, R. J.; Murphy, D. W.; Zahurak, S. Lithium insertion in Wadsley-Roth phases based on niobium oxide. *J. Electrochem. Soc.* **1983**, *130*, 2345.

(10) Griffith, K. J.; Seymour, I. D.; Hope, M. A.; Butala, M. M.; Lamontagne, L. K.; Preefer, M. B.; Koçer, C. P.; Henkelman, G.; Morris, A. J.; Cliffe, M. J., et al. Ionic and electronic conduction in $TiNb_2O_7$. *J. Am. Chem. Soc.* **2019**, *141*, 16706–16725.

(11) Preefer, M. B.; Saber, M.; Wei, Q.; Bashian, N. H.; Bocarsly, J. D.; Zhang, W.; Lee, G.; Milam-Guerrero, J.; Howard, E. S.; Vincent, R. C.; Melot, B. C.; Van der Ven, A.; Seshadri, R.; Dunn, B. S. Multielectron Redox and Insulator-to-Metal Transition upon

Lithium Insertion in the Fast-Charging, Wadsley-Roth Phase PNb_9O_{25}. *Chem. Mater.* **2020**, *32*, 4553–4563.

(12) Parui, K.; Lee, A. D.; Gandhi, S.; Butala, M. M. $R-Nb_2O_5$ has an 'idealized' V_2O_5 structure and Wadsley–Roth-like structural stability during Li-ion battery cycling. *J. Mater. Chem. A* **2023**, *11*, 5559–5567.

(13) Jesus, L. R. D.; Andrews, J. L.; Parija, A.; Banerjee, S. Defining Diffusion Pathways in Intercalation Cathode Materials: Some Lessons from V_2O_5 on Directing Cation Traffic. *ACS Energy Lett.* **2018**, *3*, 915–931.

(14) Zeng, H.; Liu, D.; Zhang, Y.; See, K. A.; Jun, Y.-S.; Wu, G.; Gerbec, J. A.; Ji, X.; Stucky, G. D. Nanostructured Mn-doped V_2O_5 cathode material fabricated from layered vanadium jarosite. *Chem. Mater.* **2015**, *27*, 7331–7336.

(15) Delmas, C.; Cognac-Auradou, H.; Cocciantelli, J.; Ménétrier, M.; Doumerc, J. The $Li_xV_2O_5$ system: An overview of the structure modifications induced by the lithium intercalation. *Solid State Ion.* **1994**, *69*, 257–264.

(16) McColl, K.; Johnson, I.; Corà, F. Thermodynamics and defect chemistry of substitutional and interstitial cation doping in layered α-V_2O_5. *Phys. Chem. Chem. Phys.* **2018**, *20*, 15002–15006.

(17) Braithwaite, J.; Catlow, C.; Gale, J.; Harding, J. Lithium intercalation into vanadium pentoxide: a theoretical study. *Chem. Mater.* **1999**, *11*, 1990–1998.

(18) Horrocks, G. A.; Braham, E. J.; Liang, Y.; De Jesus, L. R.; Jude, J.; Velaźquez, J. M.; Prendergast, D.; Banerjee, S. Vanadium K-edge X-ray absorption spectroscopy as a probe of the heterogeneous lithiation of V_2O_5: first-principles modeling and principal component analysis. *J. Phys. Chem. C* **2016**, *120*, 23922–23932.

(19) Rocquefelte, X.; Boucher, F.; Gressier, P.; Ouvrard, G. First-Principle Study of the Intercalation Process in the $Li_xV_2O_5$ System. *Chem. Mater.* **2003**, *15*, 1812–1819.

(20) Yue, Y.; Liang, H. Micro-and nano-structured vanadium pentoxide (V_2O_5) for electrodes of lithium-ion batteries. *Adv. Energy Mater.* **2017**, *7*, 1602545.

(21) Galy, J. Vanadium pentoxide and vanadium oxide bronzes—structural chemistry of single (S) and double (D) layer $M_xV_2O_5$ phases. *J. Solid State Chem.* **1992**, *100*, 229–245.

(22) Parija, A.; Prendergast, D.; Banerjee, S. Evaluation of multivalent cation insertion in single-and double-layered polymorphs of V_2O_5. *ACS Appl. Mater. Interfaces* **2017**, *9*, 23756–23765.

(23) Christensen, C. K.; Sørensen, D. R.; Hvam, J.; Ravnsbæk, D. B. Structural Evolution of Disordered $Li_xV_2O_5$ Bronzes in V_2O_5 Cathodes for Li-Ion Batteries. *Chem. Mater.* **2019**, *31*, 512–520.

(24) Delmas, C.; Cognac-Auradou, H. Formation of the ω-type phase by lithium intercalation in (Mo, V) oxides deriving from V_2O_5. *J. Power Sources* **1995**, *54*, 406–410.

(25) Ma, J.; Chen, Y.; Zhang, Y.; Song, T.; Wang, X.; Wu, X.; Law, M.-K.; Long, B. In situ K doped γ-LiV_2O_5 as long-life anode and cathode for lithium ion battery. *ACS Appl. Energy Mater.* **2022**, *5*, 10402–10408.

(26) Li, X.; Liu, C.; Zhang, C.; Fu, H.; Nan, X.; Ma, W.; Li, Z.; Wang, K.; Wu, H.; Cao, G. Effects of preinserted Na ions on Li-ion electrochemical intercalation properties of V_2O_5. *ACS Appl. Mater. Interfaces* **2016**, *8*, 24629–24637.

(27) Schofield, P.; Luo, Y.; Zhang, D.; Zaheer, W.; Santos, D.; Agbeworvi, G.; Ponis, J. D.; Handy, J. V.; Andrews, J. L.; Braham, E. J., et al. Doping-induced pre-transformation

to extend solid-solution regimes in li-ion batteries. *ACS Energy Lett.* **2022**, *7*, 3286–3292.

(28) Cheah, Y. L.; Aravindan, V.; Madhavi, S. Improved elevated temperature performance of Al-intercalated V_2O_5 electrospun nanofibers for lithium-ion batteries. *ACS Appl. Mater. Interfaces* **2012**, *4*, 3270–3277.

(29) Yu, D.; Zhang, S.; Liu, D.; Zhou, X.; Xie, S.; Zhang, Q.; Liu, Y.; Cao, G. Effect of manganese doping on Li-ion intercalation properties of V_2O_5 films. *J. Mater. Chem.* **2010**, *20*, 10841–10846.

(30) West, K.; Zachau-Christiansen, B.; Skaarup, S.; Jacobsen, T. Lithium intercalation into mixed vanadium-molybdenum oxides. *Solid State Ion.* **1992**, *53*, 356–363.

(31) Mjejri, I.; Gaudon, M.; Rougier, A. Mo addition for improved electrochromic properties of V_2O_5 thick films. *Sol. Energy Mater. and Sol. Cells* **2019**, *198*, 19–25.

(32) Duc, F.; Gonthier, S.; Brunelli, M.; Trombe, J. Hydrothermal synthesis and structure determination of the new vanadium molybdenum mixed oxide $V_{1.1}Mo_{0.9}O_5$ from synchrotron X-ray powder diffraction data. *J. Solid State Chem.* **2006**, *179*, 3591–3598.

(33) Haaß, F.; Adams, A. H.; Buhrmester, T.; Schimanke, G.; Martin, M.; Fuess, H. X-Ray absorption and X-ray diffraction studies on molybdenum doped vanadium pentoxide. *Phys. Chem. Chem. Phys.* **2003**, *5*, 4317–4324.

(34) Söllinger, D.; Karl, M.; Redhammer, G. J.; Schoiber, J.; Werner, V.; Zickler, G. A.; Pokrant, S. Modified $H_2V_3O_8$ to enhance the electrochemical performance for li-ion insertion: the influence of prelithiation and mo-substitution. *ChemSusChem* **2021**, *14*, 1112–1121.

(35) Shannon, R. D. Revised effective ionic radii and systematic studies of interatomic distances in halides and chalcogenides. *Acta Cryst.* **1976**, *32*, 751–767.

(36) Kaveevivitchai, W.; Jacobson, A. J. High capacity microporous molybdenum–vanadium oxide electrodes for rechargeable lithium batteries. *Chem. Mater.* **2013**, *25*, 2708–2715.

(37) Gruehn, R. Eine weitere neue Modifikation des niobpentoxids. *J. Less-Common Met.* **1966**, *11*, 119–126.

(38) Balakrishna, A. R. Crystallographic Design of Intercalation Materials. *J. Electrochem.* **2022**, *19*, 040802–1.

(39) Mitchell, J.; Geise, N.; Paterson, A.; Osti, N.; Sun, Y.; Fleischmann, S.; Zhang, R.; Madsen, L.; Toney, M.; Jiang, D., et al. Confined interlayer water promotes structural stability for high-rate electrochemical proton intercalation in tungsten oxide hydrates. *ACS Energy Lett.* **2019**, *4*, 2805–2812.

(40) Augustyn, V. Tuning the interlayer of transition metal oxides for electrochemical energy storage. *J. Mater. Res.* **2017**, *32*, 2–15.

(41) Boyd, S.; Ganeshan, K.; Tsai, W.-Y.; Wu, T.; Saeed, S.; Jiang, D.-e.; Balke, N.; van Duin, A. C.; Augustyn, V. Effects of interlayer confinement and hydration on capacitive charge storage in birnessite. *Nat. Mater.* **2021**, *20*, 1689–1694.

(42) Saeed, S.; Boyd, S.; Tsai, W.-Y.; Wang, R.; Balke, N.; Augustyn, V. Understanding electrochemical cation insertion into prussian blue from electrode deformation and mass changes. *Chem. Comm.* **2021**, *57*, 6744–6747.

(43) Shklover, V.; Haibach, T.; Ried, F.; Nesper, R.; Novak, P. Crystal Structure of the Product of Mg^{2+} Insertion into V_2O_5 Single Crystals. *J. Solid State Chem.* **1996**, *123*, 317–323.

(44) Kihlborg, L. Crystal Structure of $(MO_{0.3}V_{0.7})_2O_5$ of $R-Nb_2O_5$ type and a comparison with structures of V_2O_5 and V_2MoO_8. *Acta Chem. Scand.* **1967**, *21*, 2495.

(45) Toby, B. H.; Von Dreele, R. B. GSAS-II: the genesis of a modern open-source all purpose crystallography software package. *J. Appl. Crystallogr.* **2013**, *46*, 544–549.

(46) Momma, K.; Izumi, F. *VESTA3* for Three-dimensional Visualization of Crystal, Volumetric and Morphology Data. *J. Appl. Crystallogr.* **2011**, *44*, 1272–1276.

(47) Demeter, M.; Kurmaev, E.; Neumann, M.; Cherkashenko, V.; Volkov, V.; Zakharova, G., et al. Investigation of the mixed-valent system $V_{2-x}Mo_xO_5$ by XPS. International Conference on Solid State Crystals' 98: Single Crystal Growth, Characterization, and Applications. 1999; pp 296–300.

(48) Allpress, J.; Sanders, J.; Wadsley, A. Multiple phase formation in the binary system $Nb_2O_5 - -WO_3$. VI. Electron microscopic observation and evaluation of non-periodic shear structures. *Acta Crystallogr. B* **1969**, *25*, 1156–1164.

(49) Allpress, J.; Wadsley, A. Multiple phase formation in the binary system $Nb_2O_5--WO_3$: VII. Intergrowth of $H-Nb_2O_5$ and $WNb_{12}O_{33}$. *J. Solid State Chem.* **1969**, *1*, 28–38.

(50) Allpress, J. t.; Sanders, J. The direct observation of the structure of real crystals by lattice imaging. *Journal of Applied Crystallography* **1973**, *6*, 165–190.

(51) Eick, H. A.; Kihlborg, L., et al. The crystal structure of V_2MoO_8. *Acta Chem. Scand* **1966**, *20*, 1658–1666.

(52) Slade, R. C.; Ramanan, A.; West, B. C.; Prince, E. The structure of $V_9Mo_6O_{40}$ determined by powder neutron diffraction. *J. Solid State Chem.* **1989**, *82*, 65–69.

(53) Robertson, D. D.; Salamat, C. Z.; Pe, D. J.; Cumberbatch, H.; Agyeman-Budu, D. N.; Nelson Weker, J.; Tolbert, S. H. Electrochemically-Formed Disordered Rock Salt ω-$Li_xV_9Mo_6O_{40}$ as a Fast-Charging Li-Ion Electrode Material. *Chem. Mater.* **2024**,

(54) Moore, M.; Tilley, R. D.; Williams, R. The systematics of block-structure shift lattices. *Proc. R. Soc. Lond., Ser. A, Math. Phys. Eng. Sci.* **1996**, *452*, 841–857.

(55) Bielański, A.; Najbar, M. V_2O_5–MoO_3 catalysts for benzene oxidation. *Appl. Catal. A-Gen.* **1997**, *157*, 223–261.

(56) Waroquiers, D.; Gonze, X.; Rignanese, G.-M.; Welker-Nieuwoudt, C.; Rosowski, F.; Gobel, M.; Schenk, S.; Degelmann, P.; André, R.; Glaum, R., et al. Statistical analysis of coordination environments in oxides. *Chem. Mater.* **2017**, *29*, 8346–8360.

(57) Murphy, D.; Christian, P.; DiSalvo, F.; Waszczak, J. Lithium incorporation by vanadium pentoxide. *Inorg. Chem.* **1979**, *18*, 2800–2803.

(58) Shao, L.; Wu, K.; Lin, X.; Shui, M.; Ma, R.; Wang, D.; Long, N.; Ren, Y.; Shu, J. Sol–gel preparation of V_2O_5 sheets and their lithium storage behaviors studied by electrochemical and in-situ X-ray diffraction techniques. *Ceram. Int.* **2014**, *40*, 6115–6125.

(59) Langhout, J. D.; Gager, E.; Ulloa, T.; Shepard, S.; Nino, J. C.; Butala, M. M. Isovalent substitution modulates average and short-range structure in disordered rocksalt oxides. *J. Mater. Chem. A* **2024**, *12*, 32140–32153.

(60) Hu, M.; Liang, J.; Chen, X.; Wei, J.; Zhou, Z. Preparation and electrochemical performance of $Mo_6V_9O_40$ nanorods as cathode materials for Li batteries. *RSC Adv.* **2015**, *5*, 15395–15398.